Interactions among Cloud, Water Vapor, Radiation, and Large-Scale Circulation in the Tropical Climate. Part I: Sensitivity to Uniform Sea Surface Temperature Changes

KRISTIN LARSON AND DENNIS L. HARTMANN

Department of Atmospheric Sciences, University of Washington, Seattle, Washington

(Manuscript received 7 August 2002, in final form 11 November 2002)

ABSTRACT

The responses of tropical clouds and water vapor to SST variations are investigated with simple numerical experiments. The fifth-generation Pennsylvania State University–National Center for Atmospheric Research (PSU–NCAR) Mesoscale Model is used with doubly periodic boundary conditions and a uniform constant sea surface temperature (SST). The SST is varied and the equilibrium statistics of cloud properties, water vapor, and circulation at different temperatures are compared.

The top of the atmosphere (TOA) radiative fluxes have the same sensitivities to SST as in observations averaged from 20°N to 20°S over the Pacific, suggesting that the model sensitivities are realistic. As the SST increases, the temperature profile approximately follows a moist-adiabatic lapse rate. The rain rate and cloud ice amounts increase with SST. The average relative humidity profile stays approximately constant, but the upper-tropospheric relative humidity increases slightly with SST.

The clear-sky mean temperature and water vapor feedbacks have similar magnitudes to each other and opposite signs. The net clear-sky feedback is thus about equal to the lapse rate feedback, which is about -2 W m^{-2} K^{-1}. The clear-sky outgoing longwave radiation (OLR) thus increases with SST, but the high cloud-top temperature is almost constant with SST, and the high cloud amount increases with SST. The result of these three effects is an increase of cloud longwave forcing with SST and a mean OLR that is almost independent of SST. The high cloud albedo remains almost constant with increasing SST, but the increase in high cloud area causes a negative shortwave cloud radiative forcing feedback, which partly cancels the longwave cloud feedback. The net radiation decreases slightly with SST, giving a small net negative feedback, implying a stable, but very sensitive climate.

1. Introduction

How clouds and water vapor will respond to and feed back upon climate change is one of the largest uncertainties in climate prediction (Cess et al. 1996; Stocker et al. 2001). In recent years much effort has been expended in attempts to better understand the role of clouds, water vapor, and large-scale circulation in the sensitivity of the tropical climate. It has been suggested that clouds may become brighter as the sea surface temperature (SST) increases and cause a negative feedback on the temperature of the Tropics (Ramanathan and Collins 1991). The area coverage of high clouds in the Tropics may change with SST, which cloud constitute a strong feedback through the radiative effects of clouds or water vapor (Larson et al. 1999; Lindzen et al. 2001). The cloud area, cloud properties, and water vapor distribution are all strongly coupled to the large-scale circulation (Wallace 1992; Hartmann and Michelsen 1993). The ratio of the area of the Tropics dominated by subsidence is a critical quantity, because the Tropics cool to space more efficiently in the subsidence regions without thick high clouds and with low upper-tropospheric humidities (Pierrehumbert 1995). Clouds in the high SST regions of the Tropics have a small effect on the energy balance (Harrison et al. 1990) and so long as they do, changes in the area coverage by deep convective clouds only affect the top of the atmosphere (TOA) radiation balance through their role in increasing upper-tropospheric humidity (Larson et al. 1999). The net TOA cloud forcing by low clouds is negative, so that an increase in low cloudiness with increasing SST cloud produce a strong negative feedback in the Tropics (Miller 1997; Larson et al. 1999). The positive feedback of water vapor may be mitigated if the height of the tropical boundary layer decreases as the SST increases (Larson et al. 1999).

Cloud-resolving models (CRMs) with horizontal resolution of about 1 km can explicitly resolve convective organization that is important for understanding clouds in the tropical climate. CRMs have been shown to compare well with observations for tropical convective regions (e.g., Xu and Randall 1999; Wu et al. 1998). CRMs resolve the cloud mass flux, updrafts, downdrafts, and mesoscale organization associated with convection,

Corresponding author address: Dr. Kristin Larson, Department of Atmospheric Sciences, University of Washington, Box 351640, Seattle, WA 98195-1640.
E-mail: klarson@atmos.washington.edu

which are parameterized in coarser resolution models. CRM investigations help test the assumptions made in cumulus parameterizations (e.g., Xu et al. 1992). Also CRMs have been used to study cloud–radiative interaction (e.g., Li et al. 1999; Fu et al. 1995), the diurnal cycle (e.g., Liu and Moncrieff 1998), tropical convection with large-scale forcing prescribed by observations (e.g., Sui et al. 1994; Grabowski et al. 1996), theoretical studies of convection (e.g., Robe and Emanuel 1996), and climate sensitivity studies to SST (Tompkins and Craig 1999; Lau et al. 1994).

With CRM simulations, Lau et al. (1994) concluded that cloud radiative forcing is more sensitive to imposed vertical velocity forcing than to the SST. Tompkins and Craig (1999, hereafter TC99) studied the response of a three-dimensional CRM on a 60 km^2 domain with 2-km resolution to imposed SST. They found a very small cloud feedback and that the microphysical processes exhibit no significant sensitivities to temperature, except that the cloud altitude is shifted upward by a surface temperature increase. The atmospheric temperature profile tends to follow a moist adiabat corresponding to the SST, so that the lapse rate decreases with increasing SST. The relative humidity profile did not change in their experiments. TC99 also found that the altitude at which cloud ice occurred increased with increasing SST.

It is computationally very expensive to run a CRM for a large domain in three dimensions. The domain of TC99 is too small to realistically represent the two-way interaction between convection and large-scale circulations. In this study, the nonhydrostatic version of the fifth-generation Pennsylvania State University–National Center for Atmospheric Research (PSU–NCAR) Mesoscale Model (MM5), including representations of convection and clouds that interact with radiation, will be used to study interactions among clouds, large-scale circulation, and SST in the Tropics. Using this model includes more cloud physics than a two column box model or general circulation model (GCM) and it is computationally faster than a GCM or CRM. An intercomparison of models for convection during the Tropical Ocean Global Atmosphere Coupled Ocean–Atmosphere Response Experiment (TOGA COARE) over the tropical pacific shows that the MM5 with doubly periodic boundary conditions compares favorably to CRMs (Su et al. 1999; Krueger and Lazarus 1998, 1999). A doubly periodic version of the MM5 will be used to study tropical processes in isolation from the effects of the extratropics or landmasses. The primary advantage of this approach is to allow the study of large-scale interactions between regions with convection and regions with mean subsiding motion in a model framework with realistic cloud–radiative interactions.

In part one of this study, the sensitivities of the model are investigated when the model is forced by a uniform constant SST. The response of the model to constant SST is related to observations and previous detailed CRM studies to test some sensitivities of the clouds in the MM5 to uniform SST. The sensitivities of the model to uniform SST are also used as a baseline to understand the model response to the SST gradients. In part two (Larson and Hartmann 2003), SST gradients are imposed.

The horizontal and vertical distributions of total water will be solved for using prognostic cloud water equations. The model resolution will be moderately coarse (120 and 60 km), so that convective clouds will still be parameterized, but the interaction of the parameterized convection with radiation and the large-scale circulation will be explicitly included. This model can be used to investigate how the cloud and water vapor distributions interact with the large-scale circulations within the domain of the model, and how these interactions depend on SST. In the experiments described here in part one, the entire domain will be given a single SST, which will remain fixed for the entire integration. The following questions will be of interest: What fraction of the grid domain will contain convection and what fraction will be subsiding and dry, and how does this depend on the SST? As the fixed SST is changed within the range of 297–303 K, how do the fraction covered by cloud, the optical properties of the clouds, and the water vapor distribution change? Do these changes depend on the uncertain details of the model or do they result from more basic physical considerations? What implications do these changes have for climate sensitivity?

In the next section the model is described in detail. Sections 3 and 4 describe the atmospheric and energy budget sensitivities to SST. The model TOA energy budgets show sensitivities to SST that are similar to the observed sensitivities. Finally, the water vapor and cloud feedbacks are described, followed by the conclusions.

2. Model description

The essential physical processes of dynamics, cloud processes, convection, radiation, and moisture advection will be allowed to interact in the model. Descriptions of these processes as implemented in the MM5 follow in the next subsections. The last subsection describes the experiments that were conducted to address the questions of interest here.

a. Dynamics

The nonhydrostatic version of the MM5 version 2 is used in this study. A general description of the MM5 can be found in Dudhia (1993) and Grell et al. (1994). We use 24 vertical sigma levels, spaced at intervals of 0.01 (about 10 hPa) near the surface to 0.05 (about 50 hPa) above 900 hPa. The top of the model is specified to be 50 hPa.

b. Boundaries

The MM5 was modified to run with periodic boundary conditions at both north–south and east–west boundaries. In our experiments, the Coriolis force is set to zero because we are simulating the Tropics near the equator where the Coriolis force is zero. Geographical dependence of solar zenith angle is removed by using the solar zenith angle at the domain center to calculate incoming solar radiation at every grid point. The diurnal cycle of insolation is retained. We employ an upper radiative boundary condition (Klemp and Durran 1983) to allow wave energy to pass through the upper boundary without being reflected. The diffusion routines have been reprogrammed for the double periodicity and the diffusion is fourth order at all grid points.

c. Physics

The physics parameterizations used for these experiments include new parameterizations for the planetary boundary layer (PBL) and shallow cumulus convection developed at the University of Washington (UW) and the Kain–Fritsch cumulus parameterization (Kain and Fritsch 1990). The Kain–Fritsch trigger function is modified to agree with previous successful simulations of convection over the Pacific warm pool during TOGA COARE (Su et al. 1999). The threshold value of boundary layer convergence in the trigger function in the Kain–Fritsch parameterization scheme was increased by a factor of 5 in that study to force the convection to be more closely associated with resolved-scale upward motion.

The PBL and shallow convection scheme are described in Grenier and Bretherton (2001), McCaa (2001), McCaa et al. (2002, manuscript submitted to *Mon. Wea. Rev.*, hereafter MBG), and McCaa and Bretherton (2002, manuscript submitted to *Mon. Wea. Rev.*, hereafter MB). The planetary boundary layer scheme is based on Grenier and Bretherton (2001) and modified as described in McCaa (2001). Within the boundary layer, this parameterization predicts the time evolution of the turbulent kinetic energy using a 1.5-order turbulence closure model. The boundary layer scheme computes the surface fluxes according to the TOGA COARE algorithm (Fairall et al. 1996). The shallow cumulus scheme is activated for clouds of depths less than 4 km. The cloud mass flux is determined by a closure based on the turbulent kinetic energy and the convective inhibition (MBG). The PBL and shallow convection schemes simulate the surface fluxes in the trade wind regime between California and Hawaii very well (MB).

The grid-scale microphysical parameterization used in the model simulations is described in Reisner et al. (1998) and is based on Lin et al. (1983), Rutledge and Hobbs (1984), and Ikawa and Saito (1991). Cloud water, cloud ice, rainwater, and snow are all explicitly treated using this scheme. The number concentrations of cloud ice and snow are not predicted. The microphysics scheme is used without modification for these tropical experiments. The more computationally efficient simple ice scheme (Dudhia 1993) was used by Su et al. (1999).

d. Radiation

The Column Radiation Model employed by the National Center for Atmospheric Research (NCAR) Community Climate Model version 3 (CCM3) is implemented in the MM5 (Kiehl et al. 1996). The effects of trace gases are included. The ice parameterization is based on a distribution of hexagonal ice crystals (Ebert and Curry 1992). The radiation scheme is important for these experiments since they are run for more than 30 days and the dominant balance in descending regions depends strongly on the radiation over that timescale.

The random cloud overlap assumption used by the CCM3 radiation code leads to a great overestimation of total cloud fraction for multilevel clouds. The random overlap assumption is tolerated for shortwave radiative transfer, which features considerably more scattering and less absorption, but for longwave transfer, where even a single layer of cloud can have an optical depth much greater than one, a maximum random overlap assumption is implemented. Adjacent cloudy layers are assumed to have maximum overlap, while cloudy layers separated by one or more clear layers are assumed to overlap randomly (McCaa 2001).

Cumulus cloud fraction and cloud ice and water mixing ratio are provided from the UW shallow and Kain–Fritsch cumulus parameterizations. These are incorporated with the stratiform cloud amounts diagnosed from the explicit cloud ice and water fields into the cloud fraction used in the radiation code. Stratiform ice clouds are incorporated using the grid mean ice mixing ratio and assuming a cloud fraction of one in the presence of ice. To provide a smooth transition between cloudy and clear sky, and crudely represent the variability in liquid water path, a statistical cloud fraction scheme for stratiform clouds like that described in McCaa (2001) is used. It is based on an assumed normal distribution of saturation excess about its layer mean value. The standard deviation of saturation excess is specified to be 0.02 times the saturation water vapor mixing ratio.

The model has separate diagnostic values of stratiform and cumulus cloud fractions and liquid water mixing ratios that must be combined to be input into the radiation scheme. Cumulus rising into or through stratiform cloud layers are assumed to be collocated with the stratiform clouds so that the total cloud fraction is just the maximum of the stratiform and cumulus cloud fractions. The effective mean liquid water mixing ratio of the two types of cloud should avoid smearing the cumulus cloud water throughout the potentially much larger area of the stratiform cloud. It is therefore com-

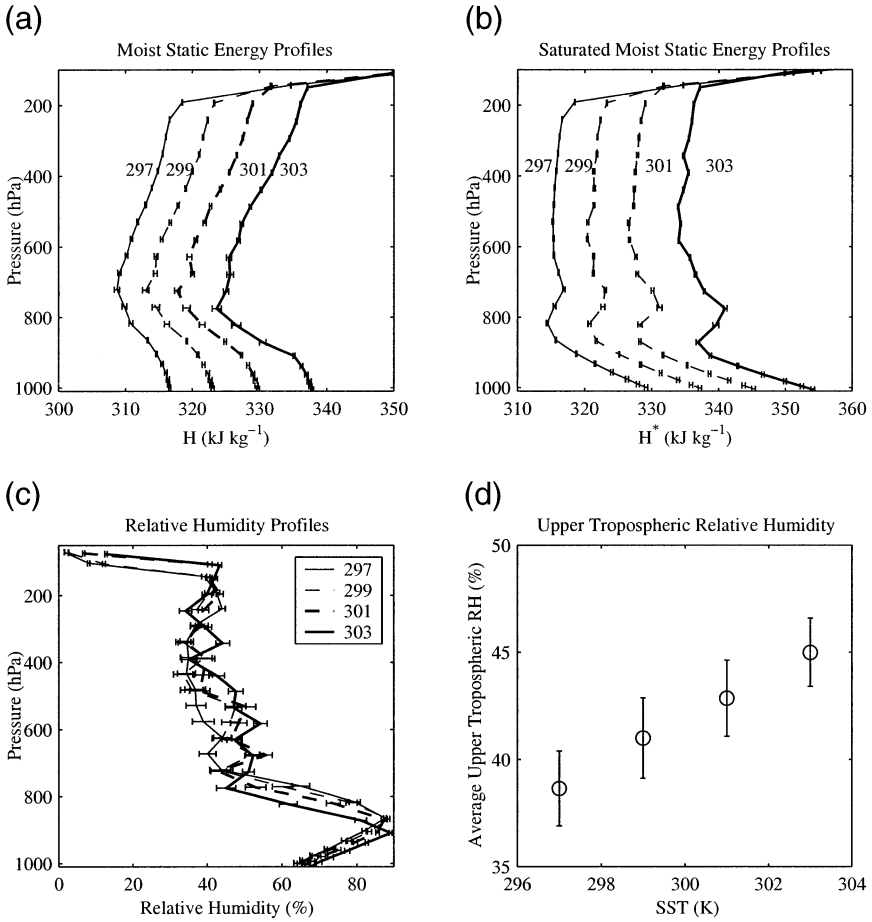

FIG. 1. Vertical profiles of (a) moist static energy, (b) saturated moist static energy, and (c) relative humidity for the four different SSTs, 297 K (thin solid), 299 K (thin dashed), 301 K (thick dashed), and 303 K (thick solid). (d) Average upper-tropospheric relative humidity vs SST. The 95% confidence intervals are indicated with error bars.

puted as a log-weighted average, which can be integrated vertically to get the cloud liquid water path.

e. Experiments

Several experiments were executed at the constant SSTs of 297, 299, 301, and 303 K, that represent a range of tropical SSTs. For each SST three different initial conditions are used to gain greater sample diversity and statistical significance. In this paper, the experiments with different initial conditions but the same SST are averaged together and 95% confidence limits are computed for the averages to show whether the model responses to SST changes are robust.

The basic experiments have a domain of 16 × 16 grid points with a grid spacing of 120 km. Additional experiments with 60-km resolution in a 32 × 32 gridpoint domain are investigated to explore the sensitivity of the results to horizontal resolution. For most of the variables we test, the response to the horizontal resolution change is no bigger than the sampling uncertainty. A statistical steady state is reached in the simulations before 60 days have elapsed. The average values for the experiments are computed from instantaneous data taken every 6 h for days 60–90 of the experiments.

3. Atmospheric sensitivities to SST

The areal coverage of high clouds increases along with the temperature, rain rate, integrated water vapor, and cloud ice as the SST increases. The upper-tropospheric humidity increases slightly as the SST increases and the amount of integrated cloud water decreases. Composites of the convective and nonconvective regions of the experiments give insights about the temperature profile, inversion height, and cloud water amounts.

a. Temperature and humidity

Figure 1 shows the moist static energy and the larger saturation moist static energy for the four different SSTs.

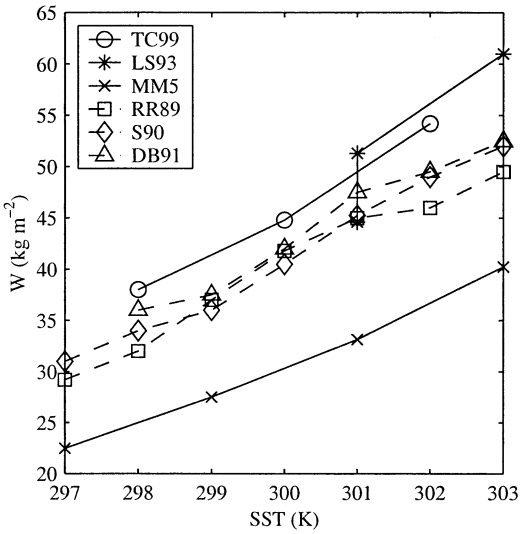

FIG. 2. Integrated water vapor vs SST for the MM5, CRMs, and observations. The model results are connected by solid lines and the observations by dashed lines. RR89 refers to the paper by Raval and Ramanathan (1989). S90 is Stephens (1990). DB91 is Duvel and Bréon (1991).

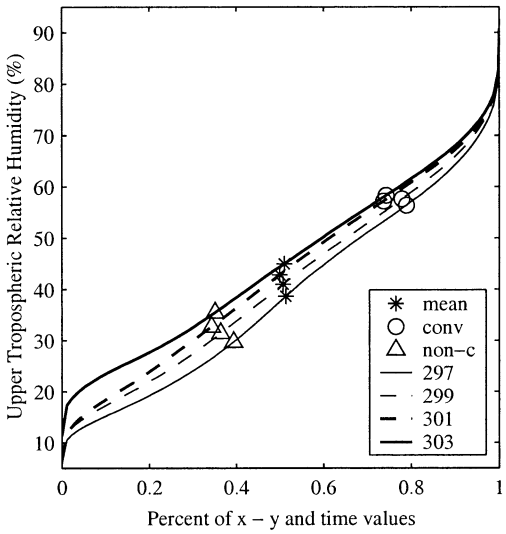

FIG. 3. The distribution of upper-tropospheric relative humidity (UTRH) for all three simulations at all grid points at every 6 h for each SST. More than 20% of the values are below 30% UTRH. The asterisks indicate the mean UTRH for each SST (297–303 K). The circles are the average UTRHs in the convective region and the triangles are the UTRH in the nonconvective region.

The saturation moist static energy is almost constant with height above the boundary layer, meaning the atmospheric temperature is following a moist adiabat. One can see that the inversion in saturated moist static energy increases in strength and moves downward with increasing SST. The relative humidity with respect to water increases linearly from about 65% at the surface to the maximum of about 90% near 875 hPa (Fig. 1c). A dry layer occurs above 700 hPa; with relative humidity values between 35% and 55% for every SST. The average relative humidity in the dry layer of the upper troposphere from 250 to 750 hPa increases slightly with increasing SST (Fig. 1d). High relative humidity above the level of the tropical inversion is associated with convection (Udelhofen and Hartmann 1995). The increase in upper tropospheric relative humidity (UTRH) would be consistent with increased high cloud amount or increasing area of convection. Because the relative humidity values are similar while the temperature increases, the specific humidity increases with increasing SST, giving strong positive water vapor feedback.

Figure 2 shows the SST versus the integrated water vapor for these experiments, observations using satellite data, and the CRM experiments of TC99 and Lau et al. (1994) and Sui et al. (1993) (hereafter the last two papers are referred to collectively as LS93). Two of the LS93 experiments were forced by rising motion and they have the highest water vapor amounts. The TC99 simulations are moister than the observations, and these MM5 simulations are drier. The dryness of these experiments is due to the smaller relative humidities and a colder mean mass-weighted temperature in the MM5. The domain for these experiments is 1920 km $\times$ 1920 km, much larger than the 3D domain of TC99 (60 km $\times$ 60 km) and still larger than the 2D domain of LS93 (768 km). Figure 3 shows the distribution of all UTRH values for all three simulations at all grid points at every 6 h for each SST. The 30-day average UTRH is less than 30% for 23% of the grid points in all of the simulations. The average *e*-folding time for the autocorrelation function at those grid points is longer than 2 weeks, showing the persistence of the dry upper troposphere. The regions of subsidence decrease the average relative humidity in the upper troposphere and are responsible for the dryness of the experiments (Held et al. 1993).

Comparison of the mean temperature among the simulations shows these simulations have colder mean mass-weighted temperatures than TC99 or LS93. An SST of 303 K in the MM5 produces almost the same mean mass-weighted temperature as an SST of 300 K for TC99 and 301 K for LS93. The coldness of the simulations may be related to weaknesses in the MM5. Dry air, from subsidence in the large domain, entrained in the PBL may contribute to overmixing in the PBL and to a cold bias in the PBL that affects the mean mass-weighted temperature and lowers the surface relative humidity (e.g., McCaa 2001). For experiments with similar mean mass-weighted temperatures, the MM5 still is drier than the CRM experiments, but the moist region of the MM5 (with net upward motion) has similar integrated water vapor to the CRM experiments with no forced vertical motion. The reason the MM5 is drier for similar mean mass-weighted temperatures is because the large domain allows for regions of subsidence and subsequent drying of the atmosphere. Salathe and Hartmann (1997) found air becomes drier the longer it is away from the moistening of deep convection in

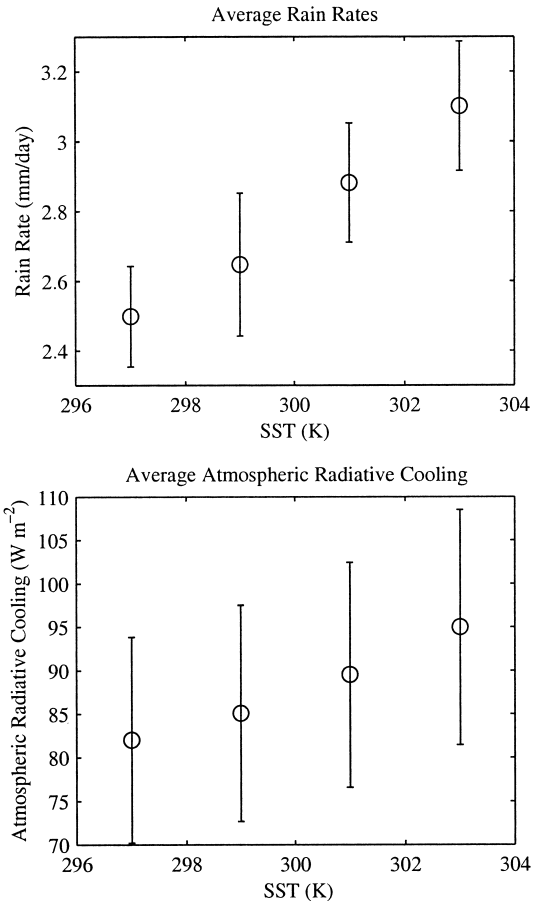

FIG. 4. Average values of (top) the rain rate and (bottom) radiative cooling for the four different SSTs. The 95% confidence intervals are noted.

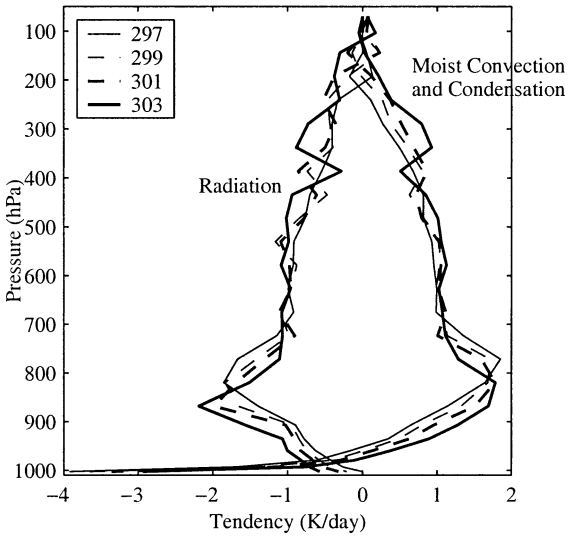

FIG. 5. Vertical profiles of temperature tendency (K day^{-1}) for the radiation and moist convection and condensation terms of the energy budget for the four different SSTs, 297 K (thin solid), 299 K (thin dashed), 301 K (thick dashed), and 303 K (thick solid).

the Tropics. The CRMs do not have as large domains so air parcels cannot spend as much time away from convection as is possible with the large MM5 domain.

One-dimensional MM5 simulations were conducted using the same physics as the coarse resolution, uniform SST simulations, except that large-scale advection was eliminated. In the 1D simulations, the cloud ice and water accumulate to much larger values than in the 3D simulations, which gives higher relative humidities and integrated water vapor amounts. The 1D simulations point to the importance of the large-scale circulation in warming and drying the atmosphere.

The Clausius–Clapeyron relation suggests that saturation vapor pressure should increase with temperature about 6% K^{-1} (Hartmann 1994, appendix B). Comparing the 303- and 297-K simulations gives an increase in integrated water vapor of about 9% K^{-1}. The model value is larger than expected because the tropospheric air temperature increases more than the SST and the relative humidity increases a little with SST also. The average precipitation rate increases about 0.1 mm day^{-1} K^{-1} of SST increase, or about 4% K^{-1} (Fig. 4). The evaporation rate must increase by the same amount as the precipitation rate in equilibrium to conserve atmospheric water vapor. The rate of change of precipitation is much less than the rate of increase of saturation vapor pressure. The reason that the precipitation does not increase at the rate of the saturation vapor pressure is that the precipitation rate over the ocean is not constrained by the source of moisture, but rather by the rate at which other processes such as radiative cooling and horizontal transport can remove heat from the atmosphere (e.g., Hartmann 1994, section 6.2). The heating that is provided to the atmosphere by latent heat release and turbulent sensible heat flux from the surface must be removed by radiation. The rate at which radiation can cool the atmosphere does not increase with temperature as rapidly as the saturation vapor pressure, and so the precipitation rate is constrained to increase more slowly than the saturation vapor pressure. The average atmospheric radiative cooling rate increases about 3% K^{-1} of SST increase (Fig. 4). Within the 95% confidence intervals, the precipitation and the radiative cooling increase at the same rate with SST, and they do not increase as fast as the integrated water vapor or the saturation vapor pressure.

The energy balance in the tropical atmosphere is between radiative cooling and moist convection and condensation (Fig. 5). Close to the surface vertical diffusion is also important, but those terms are not shown in Fig. 5. The level of strongest radiative cooling is near the steepest gradient in specific humidity between 800 and 900 hPa. The altitude of this level decreases with increasing SST. The upper-tropospheric level where the radiative cooling rate is 0.5 K day^{-1} rises as the SST increases, but the temperature there remains constant at approximately 212 K. Radiative cooling above this level

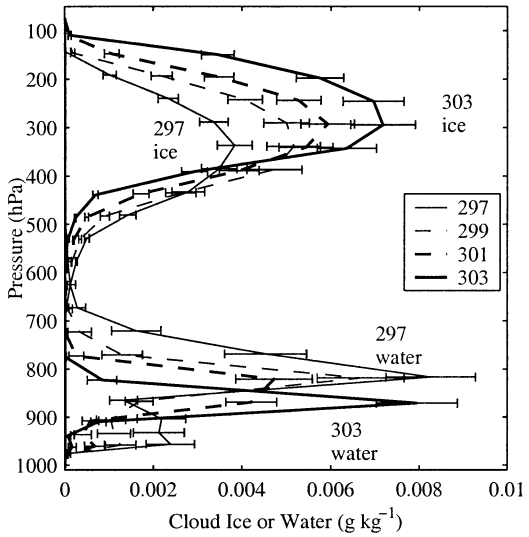

FIG. 6. Vertical profiles of cloud water and cloud ice (g hg^{-1}) for the four different SSTs, 297 K (thin solid), 299 K (thin dashed), 301 K (thick dashed), and 303 K (thick solid). The 95% confidence intervals are noted.

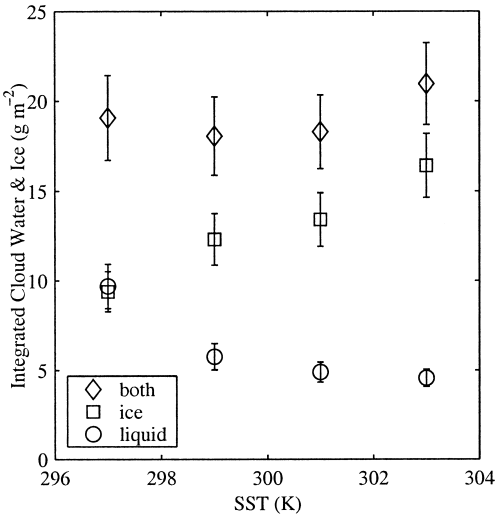

FIG. 7. Average values of the integrated cloud liquid water (liquid), integrated cloud ice (ice), and the sum of all cloud water (both). The 95% confidence intervals are noted.

is inefficient because the water vapor amount is so small in the upper troposphere (Hartmann et al. 2001a). The fact that the temperature is nearly constant at the level where the radiative cooling rate reaches 0.5 K day^{-1} implies that the emission temperature of anvil clouds may remain constant during climate change (Hartmann and Larson 2002).

Figure 6 shows that the cloud ice profile is peaked in the upper troposphere. The peak values are larger and occur at higher levels as the SST increases. The cloud ice profile also peaks at higher levels for warmer SSTs in TC99 and LS93. The cloud water profiles do not show a discernible trend in magnitude, but the peak values occur at lower levels for higher SSTs, consistent with the lowering of the level of maximum radiative cooling with SST. The average values of the integrated liquid water and ice amounts are shown in Fig. 7. As the SST is increased the liquid water decreases and the ice increases. In the warmer SST cases ice is formed instead of liquid water in the convective region and most of the cloud liquid water is found in regions of subsidence. The sum of the integrated cloud ice and liquid water is approximately constant with SST. More ice and less liquid water at higher SST is consistent with deeper convection reaching higher in the troposphere.

The cloud water and cloud ice values can be used to define the cloud fraction. The cloud-top pressure is defined here as the level where the visible optical depth reaches 0.1. If the cloud optical depth is less than 0.1, it is grouped in the clear-sky category. Following the International Satellite Cloud Climatology Project (ISCCP) definitions (Schiffer and Rossow 1985; Rossow and Schiffer 1999), high clouds are defined to have tops at or above 440 hPa and the low clouds have tops at or below 680 hPa, while the middle clouds have tops between those values. Figure 8 displays the percentage of the area where clear skies, high clouds, middle clouds, and low clouds are present, using radiative fluxes output every 30 min and averaging over the third 30 days of the experiments. The high cloud cover increases with increasing SST, consistent with the increase of integrated cloud ice. The areas of middle clouds and low clouds decrease less than the area of high clouds increases with increasing SST, so that the clear fraction decreases with SST. The decrease of middle and low clouds may mean that the lower clouds are overlapped

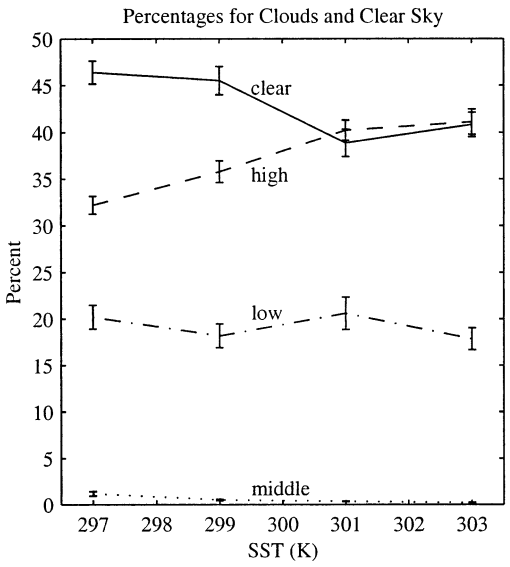

FIG. 8. Clear-sky, high, middle, and low cloud percent amount for the constant SST experiments. The line type denotes the cloud type. The 95% confidence intervals are noted.

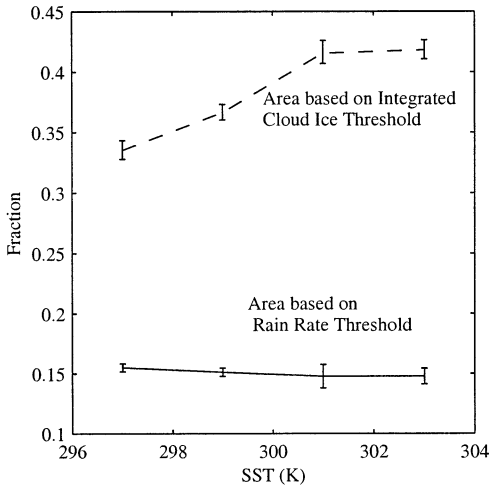

FIG. 9. Fraction of the domain above the convective threshold for integrated cloud ice, and rain rate. The convective threshold for integrated cloud ice is 1 g m^{-2}. The convective threshold for rain rate is 4 mm day^{-1}. The error bars represent the 95% confidence limits.

by the increasing amounts of high clouds, it does not necessarily mean the amounts of lower clouds are decreasing. The probability of seeing a middle level cloud in the model is very low.

b. Convective area fraction

The ratio of the convective area to the subsidence area is an important concept in the analysis of climate sensitivity (e.g., Pierrehumbert 1995; Larson et al. 1999; Lindzen et al. 2001). The convective area can be defined as a region of high relative humidity with high clouds and upward motion. The subsidence region is defined by downward vertical velocities, and often contains lower UTRH. Low clouds are present, but optically thick high clouds are noticeably absent in this region. We have investigated several objective methods of defining the convection and nonconvective regions.

The rain rate, and the integrated cloud ice are variables that can be used as indices to define the convective regions. Because the convective regions move around within the model domain, the average value of these variables in space or time will not describe the convective region accurately. Rather, these variables are used to define the convective area every 6 h for days 60–90 of the experiment. Integrated cloud ice and rain rate are used to define convective areas by choosing a threshold value and finding the percent of the domain that is above that value.

High clouds with optical depth greater than 0.1 can be used to indicate the convective region. An integrated cloud ice threshold of 1 g m^{-2} gives convective area fractions that are within 1% of the high cloud amounts defined with the optical depth criterion (Fig. 9). The convective area increases with SST at a rate of 1.5% K^{-1} for the integrated cloud ice.

If a threshold rain rate of 4 mm day^{-1} is used, then the rain rate indicates deep convection. The drizzle in the subsidence region produces a rain rate that is at least an order of magnitude smaller than the rain rate typically found in the deep convective parts of the domain. Because some parts of the domain are in the convective region with high clouds and high humidity but not rain, the convective area using the rain-rate threshold is much less than for the integrated cloud ice threshold, about 15% (Fig. 9). The fraction of the domain where it is raining does not change very much with increasing SST.

The results are dependent on the representation of convection in the model. Deep convection occurs via the Kain–Fritsch cumulus parameterization, which controls the trigger function, cloud updraft and downdraft representations, and the cloud mass flux closure assumptions. LS93 and TC99 describe few changes in convection due to SST changes. In LS93, this is perhaps related to the constant-forced vertical motion while the SST is changed. The constant convective area defined by the rain-rate threshold suggests that the area with active convection remains constant with increasing SST, consistent with the CRMs. The increase of cloud ice, decrease of cloud water, and stronger inversion are consistent with increasingly deep convection with increasing SST, a feature not found in LS93 and TC99, but possible in MM5 simulations with SST gradients.

Using the thresholds of integrated cloud ice and rain rate, two sets of composites are made of the average values in the convective and nonconvective regions. These composites show that the relative humidity is higher in the convective (high cloud, raining) regions than in the nonconvective regions (Fig. 10a). The UTRH has a stronger increase with respect to SST in the nonconvective region than the convective region (Fig. 10b). The convective and nonconvective UTRH values are also marked in the distribution of UTRH in Fig. 3.

The average vertical velocity is upward in the convective regions and downward in the nonconvective regions, as expected (Fig. 10c). In the nonconvective region, subsidence warming balances radiative cooling. Because the lapse rate decreases with increasing SST and the radiative cooling increases in association with increases of humidity of the atmosphere, these effects offset each other and the nonconvective vertical velocity is similar with changing SST. The larger decrease in the vertical velocity profiles of the convective region is due to the increase in convective area with increasing SST. The large-scale circulation in these simulations is constrained by the balance between radiative cooling and subsidence warming in the nonconvective region.

Composites for stratiform cloud water in the nonconvective region defined by the cloud ice threshold are shown in Fig. 11a. The nonconvective cloud water profiles show a definite downward shift of the layer with maximum cloud water as the SST is increased. This result agrees well with Larson et al. (1999), who pre-

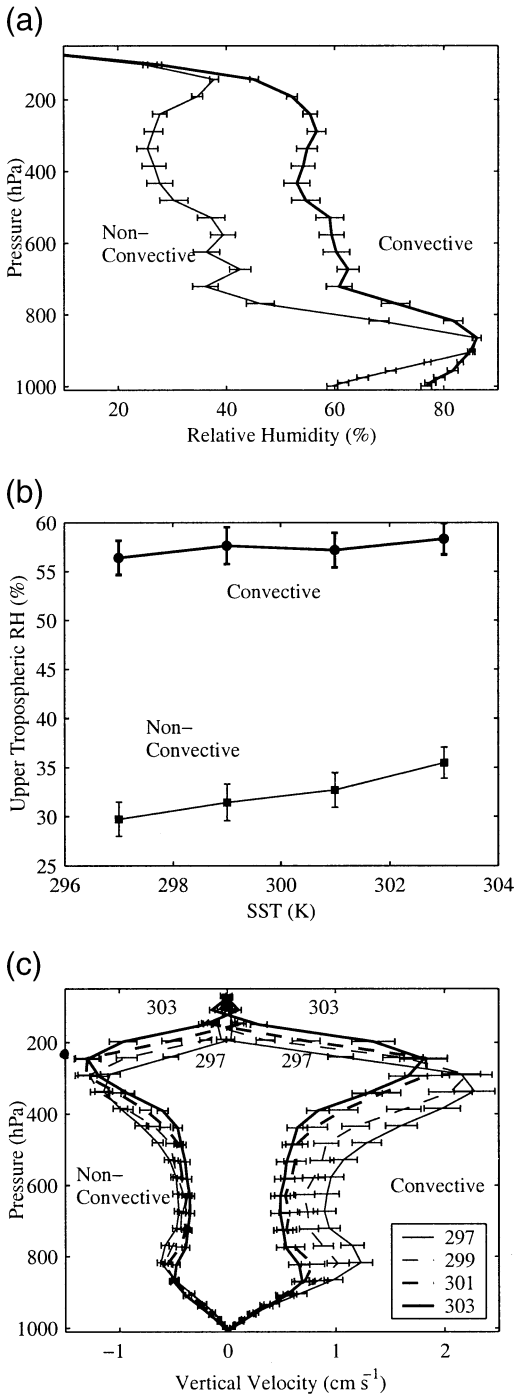

FIG. 10. (a) Relative humidity, (b) upper-tropospheric relative humidity, and (c) vertical velocity for the convective and nonconvective regions for composites based on integrated cloud ice. Four different SSTs and the 95% confidence limits are noted, 297 K (thin solid), 299 K (thin dashed), 301 K (thick dashed), and 303 K (thick solid).

dicted the boundary layer height in the subsiding region should decrease with an increasing value of the moist adiabat above the layer. Larson et al. (1999) showed that the lowering of the boundary layer height with increasing SST caused a significant reduction in the greenhouse effect of the atmosphere.

The difference in temperature profile for the convective and nonconvective regions can be seen in Fig. 11b. Only the lower portion of the atmosphere is shown because the temperature profile is very uniform across the entire domain above 700 hPa. It is a common trait of the Tropics that the horizontal temperature gradient is small in the upper troposphere. The convective profiles have a colder temperature near the surface and a relatively constant lapse rate in the lower troposphere. The nonconvective profiles have a warmer temperature near the surface and a weaker lapse rate suggestive of an inversion between 800 and 900 hPa. The inversion moves downward and gets stronger with increasing SST, which is consistent with the lowering of the cloud water in the nonconvective region.

4. Comparison with observed sensitivities of energy budget to SST

The implications of these simulations for climate sensitivity can be examined by considering the sensitivity of the outgoing longwave radiation (OLR), net absorbed shortwave radiation (SWI), and net radiation to the imposed SST. In addition we can consider the relative roles of different sky types: high clouds, low clouds, clear skies, and the average of all sky types. Figure 12 shows the OLR, absorbed shortwave, and net incoming radiation for different sky types as functions of SST. The OLR of the high clouds decreases with increasing SST, because the cloud tops become slightly colder and the ice optical depth increases. The high cloud-top temperature where the ice optical depth reaches 0.1 is approximately 200 K for all the simulations (Hartmann and Larson 2002). The OLR for clear skies increases because the SST and air temperatures increase. The OLR for low clouds increases because the height of the temperature inversion decreases with increasing SST and the low cloud-top temperature increases faster than the SST. The mean OLR decreases slightly with SST because the cloud amount increases and the high cloud OLR decreases with SST for all of the experiments. Earth Radiation Budget Experiment (ERBE) values (averaged from 1985 to 1987, 20°N–20°S, 140°E–90°W) of OLR for average and clear-sky conditions are 256 and 290 W m^{-2}, respectively, very comparable to the results of these simulations.

a. Accounting for diurnal variations

In order to properly calculate the effect of cloud types on the solar and net radiation, the diurnal variation of insolation and cloud amount must be handled carefully. The high and low clouds in the model both have a diurnal cycle in their area coverage. The high clouds have a diurnal maximum of area coverage near midnight and a minimum near noon. The diurnal cycle in the area

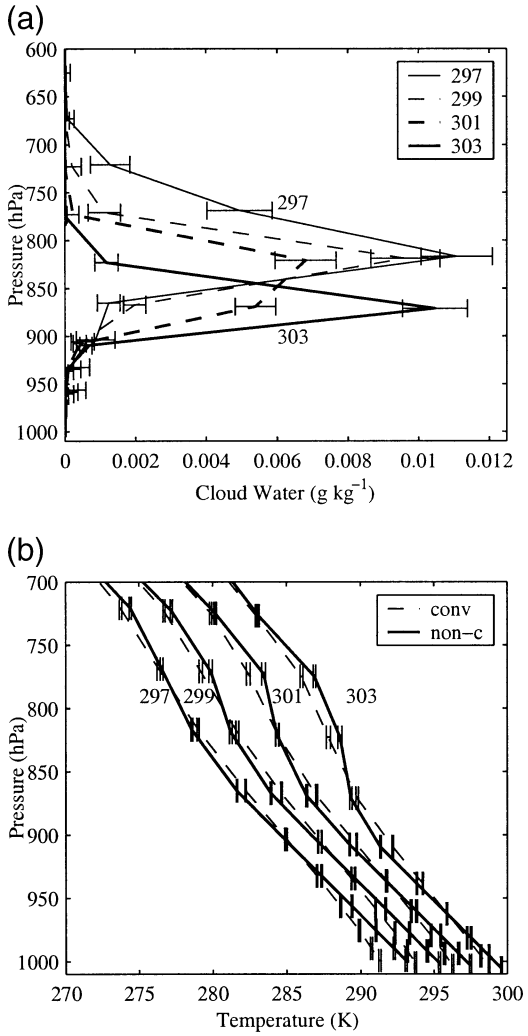

FIG. 11. Vertical profiles of (a) cloud water and (b) temperature for the convective and nonconvective regions for composites based on integrated cloud ice. Four different SSTs and the 95% confidence limits are noted, 297 K (thin solid), 299 K (thin dashed), 301 K (thick dashed), and 303 K (thick solid). For the cloud water, only the nonconvective profiles are shown. For the temperature, the convective profile is dashed and the nonconvective profile is solid.

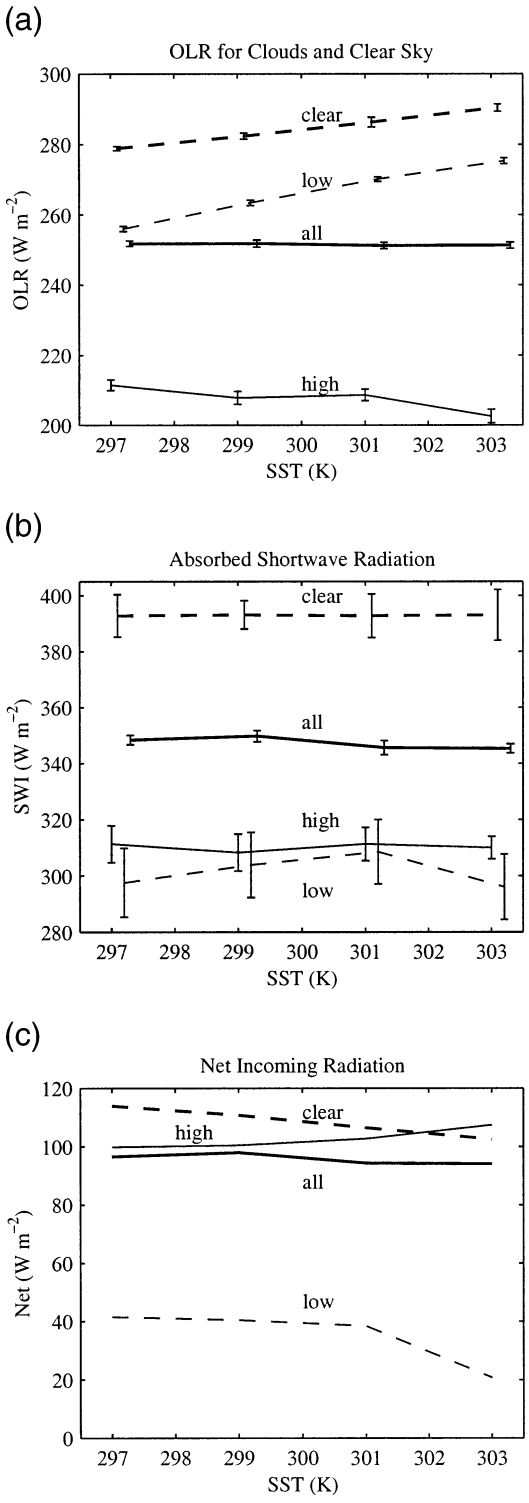

FIG. 12. (a) OLR, (b) net absorbed shortwave radiation, and (c) net incoming radiation at the top of the atmosphere. The 95% confidence intervals are noted.

coverage by high clouds has a peak-to-peak amplitude of about 8%, around a mean value of 41% for the 303-K SST case. International Satellite Cloud Climatology Project (ISCCP) data show a high cloud percentage that exceeds 40% in a large area over the west Pacific warm pool (e.g., Hartmann et al. 2001b). Geosynchronous satellite data show a nighttime maximum and daytime minimum of high clouds over the tropical ocean, although the diurnal cycle varies greatly from place to place (e.g., Albright et al. 1985; Hartmann and Recker 1986; Janowiak et al. 1994; Chen and Houze 1997).

The model produces a fairly realistic diurnal cycle of low clouds. The low clouds in the experiments have a maximum area extent just after sunrise, and a minimum in midafternoon, with about a 10% peak-to-peak vari-

TABLE 1. The sensitivity of radiative energy balance components to SST: HM93 vs experiment estimates. The ''Pacific'' is defined as the ocean areas falling within the longitude range of 120°E–70°W. The units on all the quantities are W m^{-2} K^{-1}. Subscript CS indicates a clear-sky value. OLR = outgoing longwave radiation at the top of the atmosphere, G = total greenhouse effect of atmosphere = σT_S^4 − OLR, G_a = clear atmosphere greenhouse effect = σT_S^4 − $\mathrm{OLR}_{\mathrm{CS}}$, C_l = longwave forcing by clouds = $\mathrm{OLR}_{\mathrm{CS}}$ − OLR, SWI = absorbed solar radiation, C_s = shortwave cloud forcing = $\mathrm{SWI}_{\mathrm{cs}}$ − SWI, R^{∞} = net radiation at the top of the atmosphere. Italics represent values for which the explained variance is less than 50%.

Variable	5°N–5°S 180°–90°W	10°N–10°S Pacific	20°N–20°S Pacific	30°N–30°S Pacific	Experiments
$4\sigma T_S^3$	6.2	6.2	6.1	6.1	6.1
$\frac{d\mathrm{OLR}}{dT_S}$	−20.5	−12.5	−0.7	2.8	*−0.1*
$\frac{d\mathrm{OLR}_{\mathrm{CS}}}{dT_S}$	−2.6	−1.0	1.6	1.8	1.7
$\frac{dG}{dT_S}$	26.7	18.6	6.9	3.3	6.2
$\frac{dG_a}{dT_S}$	8.7	7.1	4.6	4.3	4.4
$\frac{dC_l}{dT_S}$	18.0	11.5	2.3	−1.0	1.8
$\frac{d\mathrm{SWI}}{dT_S}$	−21.0	−12	−0.7	1.9	*−0.7*
$\frac{d\mathrm{SWI}_{\mathrm{CS}}}{dT_S}$	0.6	0.4	0.1	0.4	*0.0*
$\frac{dC_S}{dT_S}$	−21.6	−12.5	−0.8	1.1	*−0.7*
$\frac{dR^{\infty}}{dT_S}$	−0.5	0.3	0.0	−0.9	*−0.6*
$\frac{dR^{\infty}_{\mathrm{CS}}}{dT_S}$	3.1	1.4	−1.5	−1.4	−1.7
$\frac{dC_S}{dT_S} + \frac{dC_l}{dT_S}$	−3.7	−1.0	1.5	0.6	*1.1*

ation in the cloud cover. Observations from ISCCP, assuming random overlap of high clouds over low clouds, show a maximum low cloud area coverage at 3 A.M. local time and a minimum at 3 P.M. local time, with a maximum variance over the eastern Pacific of 10% (Rozendaal et al. 1995).

Because the cloud fraction varies during the day, some care must be taken to obtain appropriate sensitivities from the numerical experiments. In order to make the cloud fractions for shortwave radiation consistent with those for longwave, we have multiplied the shortwave radiation values for each sky cover (e.g., high cloud, low cloud, and clear sky) by the average sky cover divided by the insolation-weighted sky cover. These values are computed by summing over the 48 half-hour sampling periods during the day. This factor adjusts the values so that the clear sky, high and low cloud values can be linearly combined to make the correct average shortwave flux.

The absorbed shortwave flux does not show significant sensitivity to the SST for any of the sky types or for the sum of all sky types (Fig. 12b). ERBE observations show the average SWI is about 321 W m^{-2} and the clear-sky average is 366 W m^{-2} (averaged from 1985 to 1987, 20°N–20°S, 140°E–90°W), both values are comparable to the results from these simulations. The net radiation has a weaker dependence on SST than do OLR and SWI (Fig. 12c). The clear-sky net radiation decreases slightly with increasing SST because clear-sky OLR increases with SST as the net result of the water vapor, temperature, and lapse rate feedback. The high cloud net radiation has a small positive increase with increasing SST and the net radiation for low clouds decreases with increasing SST, both because of the OLR sensitivity. The average net radiation has a very small decrease with increasing SST.

b. Comparison to observations

The sensitivity of the TOA radiative fluxes to SST was estimated from ERBE observations in HM93 by comparing the changes of radiation quantities and SST between La Niña and El Niño years averaged over large regions of the Pacific Ocean. To find the sensitivities, the difference in the radiative quantity between La Niña and El Niño is divided by the change in SST between La Niña and El Niño. Table 1 compares estimates from HM93 with estimates obtained from least squares fits

of the radiation budget values from the model to the imposed SST for the 12 coarse resolution experiments. Values for which the explained variance is less than 50% are in italics, this is most common when the slope is close to zero. The table shows these model experiments give similar sensitivities to those obtained by averaging observations from 20°N–20°S or 30°N–30°S in the Pacific Ocean region. It is appropriate to compare observations averaged over the rising and sinking branches of the Hadley and Walker Circulations to averages of the model domain in which the vertical motion averages to zero.

Changes of the energy budgets due to SST in these simulations show blackbody radiation and the atmospheric greenhouse effect are more sensitive to SST than the longwave and shortwave cloud forcings (Table 1). Lau et al. (1994) found similar sensitivities to SST using CRM simulations with SSTs of 301 and 303 K forced with rising motion. Using uniform SST CRM simulations with and without forced rising motion, Lau et al. (1994) calculated very large sensitivities of the shortwave and longwave cloud forcing to rising motion. These large cloud sensitivities are similar to the large values of cloud sensitivities in Table 1 when the observations are averaged from 5°N to 5°S or 10°N to 10°S. The MM5 simulations don't have imposed vertical motion, but averages for the entire simulation can be compared to averages over areas with rising motion in the simulations to assess sensitivities to rising motion similarly to Lau et al. (1994).

Since the convective and nonconvective regions defined with the integrated ice amount have mean vertical velocities that are upward and downward, respectively, we can use the convective and nonconvective regions to estimate sensitivity to vertical motion. Using this definition, the MM5 also shows shortwave and longwave cloud forcing at the TOA have large sensitivities to vertical motion. At the surface, these simulations and Lau et al. (1994) find the shortwave radiation sensitivity to rising motion is bigger than any other sensitivity. Latent heat flux shows different sensitivities, probably because the latent heat fluxes are based on different minimum wind speeds and gustiness parameterizations. For both models, the TOA cloud forcing is much more sensitive to the vertical motion than to the SST.

5. Cloud, water vapor, and lapse rate feedbacks

The model experiments can be used to estimate values of the climate feedback parameter and its dependence on various feedback processes that operate within the model. The feedback parameter measures the ratio of the equilibrium temperature change (dT_s) in response to an imposed climate forcing (dQ) [e.g., Hartmann 1994, Eq. (9.2)],

$$\frac{dT_s}{dQ} = \lambda. \tag{1}$$

TABLE 2. Longwave clear-sky feedback factors (SST = 299 K) obtained from offline calculations using averaged model results and a radiative transfer model (units are W m^{-2} K^{-1}).

Type of feedback	Convective	All	Nonconvective
Water vapor	4.13	4.11	3.75
Temperature	−4.03	−4.07	−4.10
Lapse rate	−1.87	−1.77	−1.71
Total	−1.78	−1.72	−2.06

Since the SST is fixed in these experiments, the feedbacks must be evaluated using the inverse technique as in Cess et al. (1996), Zhang et al. (1994), TC99 and others, where the SST perturbation is imposed and the radiative response at the top of the atmosphere is examined after the atmosphere has reached a new thermodynamic equilibrium. The net radiation at the top of the atmosphere R,

$$R = \text{SWI} - \text{OLR}, \tag{2}$$

is substituted for Q in Eq. (1) and the sensitivity parameter, λ, can be estimated.

As the SST is perturbed, the mean temperature (represented by subscript T), the lapse rate (L), the water vapor amount (w), and the cloud properties of the atmosphere (c) all change. To isolate the effect of each process, the overall atmospheric feedback in the experiments is partitioned linearly (assuming no interaction between the feedback effects) as follows:

$$\lambda = \frac{dT_s}{dR} = \left[\left(\frac{\partial R}{\partial T_s}\right)_T + \left(\frac{\partial R}{\partial T_s}\right)_C + \left(\frac{\partial R}{\partial T_s}\right)_W + \left(\frac{\partial R}{\partial T_s}\right)_L\right]^{-1}$$
$$= (\alpha_T + \alpha_C + \alpha_W + \alpha_L)^{-1}, \tag{3}$$

where, for example, α_w is the rate of change of the radiative forcing with respect to the SST, when only the water vapor profile is allowed to change and all other parameters remain fixed. To separate the effects of mean temperature, lapse rate, and water vapor, the radiation scheme is run offline for a single atmospheric column using the average profiles from the experiments (e.g., Hansen et al. 1985). The feedback factors are computed for the convective (high cloud) and nonconvective (clear sky, low and middle clouds) averages based on radiation outputs every 30 minutes as well as the overall average. An error is associated with using the average profiles instead of the means of the radiative quantities, but it is small here. Nonlinear interactions between the feedback factors are not detected with this method. Only the longwave portion of the feedback factors was computed offline, because the shortwave effects are very small for clear skies.

Tables 2 and 3 show the longwave sensitivity parameters estimated by offline calculations using the central SST values of 299 and 301 K, respectively. The water vapor feedback is large and positive. It is largest for the total domain and the convective region because the area of the moist convective region increases with SST and

TABLE 3. Longwave clear-sky feedback factors (SST = 301 K) obtained from offline calculations using averaged model results and a radiative transfer model (units are W m^{-2} K^{-1}).

Type of feedback	Convective	All	Nonconvective
Water vapor	4.72	4.56	4.23
Temperature	−4.10	−4.13	−4.17
Lapse rate	−2.55	−2.43	−2.35
Total	−1.93	−2.01	−2.29

the convective region has the highest water vapor content. The smaller feedback in the nonconvective region is due to the decrease in the inversion height with increasing SST. The feedback is stronger for the 301-K base SST, because the specific humidity is higher there and the change in specific humidity with SST increases with increasing temperature. The water vapor feedback is smaller than found in TC99, perhaps because the upper-troposphere relative humidity and the integrated water vapor amount are lower in this model. The upper-troposphere relative humidity is lowest in regions of subsidence, and the large domain of these experiments permits regions of persistent subsidence to develop that might not occur in the smaller domain of TC99.

The temperature feedback is found by keeping the specific humidity and lapse rate constant and changing the temperature everywhere by the same amount as the SST. The temperature feedback, which is basically the increase in the Planck function for a uniform temperature change, is approximately canceled by the effect of the water vapor amount acting alone.

The lapse rate feedback is found by using the equilibrium temperature profiles from the perturbation experiments and subtracting the SST perturbation value from the entire temperature profile, then computing the radiative fluxes using the base SST and specific humidity profile. It is negative because the moist-adiabatic lapse rate decreases for warmer SST. The lapse rate effect is slightly stronger in the nonconvective region because of the temperature inversion. Because the water vapor and temperature effects nearly cancel, the net clear-sky feedback is negative and approximately equal to the contribution from lapse rate feedback.

Table 4 shows the feedback factors obtained from a linear fit of the model experiment results to the imposed SST. The convective region is defined to contain high clouds. Values where the explained variance of the linear fit is less than 0.5 are italicized. The longwave values agree well with the values obtained from the offline radiative transfer calculations shown in Tables 2 and 3. The clear-sky shortwave feedback factor is small in all regions.

To examine the cloud feedback effect, the net radiation R is separated into its clear and cloudy sky components to calculate the cloud radiative forcing (Charlock and Ramanathan 1985 and others),

$$\mathrm{CRF} = R - R_{\mathrm{CS}}, \tag{4}$$

TABLE 4. Feedback factors obtained from the TOA fluxes of the 12 uniform SST experiments (units are W m^{-2} K^{-1}). Values where the explained variance of the linear fit is less than 0.5 are italicized.

Type of feedback	Convective	All	Nonconvective
Total clear-sky (LW)	−1.73	−1.68	−1.95
Total clear-sky (SW)	0.09	*0.03*	*0.01*
α_c (LW)	3.02	1.79	−0.37
α_c (SW)	*−0.14*	*−0.70*	*0.15*
α_c (net)	2.89	*1.09*	*−0.22*
Total LW feedback	1.29	*0.10*	−2.32
Total SW feedback	*−0.04*	*−0.67*	*0.16*
Total net feedback	1.25	*−0.56*	*−2.16*

where R_{CS} represents the net radiative flux at the TOA for the clear-sky regions. We define,

$$\alpha_c = \frac{\Delta \mathrm{CRF}}{\Delta T_s}. \tag{5}$$

The difference between the clear and cloudy sky TOA fluxes in the model gives the cloud feedback that is summarized in Table 4 for longwave, shortwave, and total radiation.

The longwave cloud feedback factor is strongly positive in the convective region because the clear-sky OLR increases and the high cloud OLR decreases slightly with increasing SST. The low clouds in the nonconvective region actually have a slightly negative feedback, because the low cloud-top height slightly decreases with increasing SST (Fig. 13). The shortwave cloud feedback factor is close to zero for the convective and nonconvective regions, but negative for the overall average. The cloud optical depth in the two regions does not change significantly with temperature. But because the high cloud area increases with SST, a significant negative shortwave cloud feedback occurs for the whole model domain. The high cloud coverage increase also contributes about half of the positive longwave cloud feedback for the whole domain. Clouds produce a net positive feedback overall and in the convective region. The nonconvective region has a small negative cloud feedback.

The net clear-sky feedback in these simulations is negative because of the longwave effects. The cloud feedbacks are positive in the experiments, mostly because the clear-sky OLR increases and the high cloud OLR decreases with increasing SST. For the whole domain, the net feedback is small. For these experiments, the TOA radiative fluxes are insensitive to the SST, implying a very sensitive climate.

6. Summary and conclusions

Experiments performed with uniform constant SST, parameterized convection, predicted cloud properties, and interactive radiation are able to simulate the observed sensitivity of tropical radiation budget quantities to imposed SST estimated from El Niño events. Since the model produces responses to SST of clear-sky fluxes

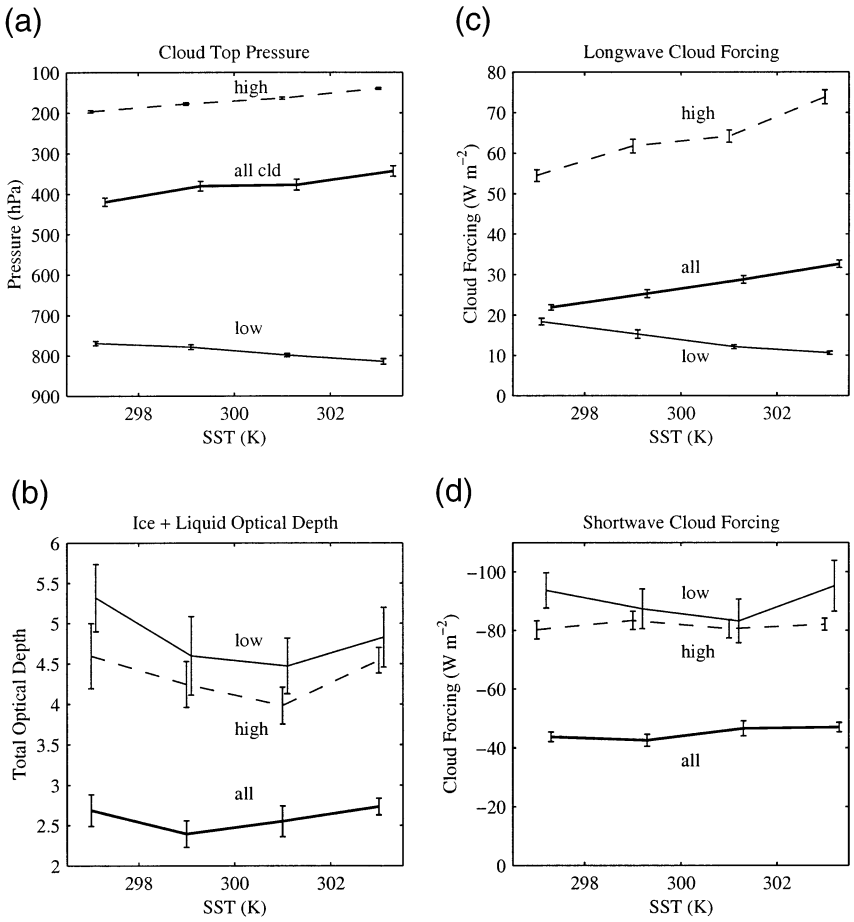

FIG. 13. (a) Cloud-top pressure, (b) cloud visible optical depth, (c) longwave cloud forcing, and (d) shortwave cloud forcing for the constant SST experiments. The 95% confidence intervals are noted.

and cloud forcing that are similar to observations, we have some confidence in the basic cloud and radiation physics incorporated in the model.

For the thermodynamic variables, the temperature profiles follow an essentially moist-adiabatic profile with increasing SST. The relative humidity profile does not show a systematic response to increased SST, though the UTRH increases slightly. The altitude of the tropical inversion and the associated boundary layer cloud tops both decrease with increasing SST, as predicted in Larson et al. (1999). The altitude of the cloud ice maximum increases with SST, as is also found in CRMs, and the average rain rate and latent heat flux both increase with SST.

It is important to remember that these simulations depend on cumulus parameterization. These coarse resolution simulations, whose fast computation is useful for simulations of the entire Pacific, show agreement with the observed sensitivity of clouds to SST, but a colder, drier mean state than other radiative–convective equilibrium CRMs. The mean state may be biased by weaknesses in the model. The increase of the high cloud amount and the size of the convective region with the increase of SST is difficult to validate observationally. A simple two box model predicted a warmer mean temperature with increases in the warm pool size, which is consistent with this model (Larson et al. 1999). In this model, the total integrated cloud water and the convective area based on rain rate are insensitive to the SST, in general agreement with CRMs (TC99; Lau et al. 1994).

The total clear-sky feedbacks are similar in the convective and nonconvective regions and similar to values in other models (TC99; Zhang et al. 1994; Weaver et al. 1994). The water vapor and mean temperature clear-sky feedbacks both have magnitudes close to 4 W m^{-2} K^{-1}, and tend to cancel each other out. The lapse rate feedback is about -2 W m^{-2} K^{-1}, similar to the net clear-sky feedback, and is slightly higher than the value found in TC99. Observations (Lau et al. 1997) show an OLR sensitivity of 1.8 to 2.5 W m^{-2} K^{-1} for subsidence and clear-sky conditions, which is similar to the net clear-sky feedback found in these experiments.

The longwave cloud forcing increases because the

high cloud OLR decreases (1.3 W m^{-2} K^{-1}) and the clear-sky OLR increases (1.7 W m^{-2} K^{-1}) with increasing SST. The ice optical depth is increasing with SST and the temperature at the level with the maximum cloud ice concentration is approximately constant, causing the emitting temperature for the high clouds to decrease and produce the small decrease in high cloud OLR as the SST increases. Bony et al. (1997) showed that observed cloud-top heights and longwave cloud forcing increase with SST. The increase of longwave cloud forcing with SST is a positive feedback. The total visible optical depth of the high and low clouds do not show significant sensitivities to SST. Observations also show very weak dependence of cloud optical depth on SST for regions without strong vertical forcing (Bony et al. 1997). The high cloud fraction increases with SST, which produces a positive longwave cloud feedback and a negative shortwave cloud feedback. These effects nearly cancel each other because the net high cloud forcing is close to zero.

The positive cloud feedback and the negative clear-sky feedback are about equal. Together these effects produce a model system in which the TOA radiative fluxes are not very sensitive to the SST, implying a very sensitive climate. The sensitivities calculated in these experiments imply that an external forcing of 1 W m^{-2} would force an SST change of 1.8 K. SST gradients, vertical motions, and energy exchanges to the extratropics are not considered here and could affect the sensitivity of tropical climate. In part two of this work, the cloud and water vapor feedbacks are studied in an environment with imposed SST gradients.

Acknowledgments. This research was supported by NASA Grant NAGS5-10624. The help of Jim McCaa and Marc Michelsen was invaluable. Chris Bretherton and two anonymous reviewers provided insightful comments on the manuscript.

REFERENCES

Albright, M. D., E. E. Recker, R. J. Reed, and R. Dang, 1985: The diurnal variation of deep convection and inferred precipitation in the central tropical Pacific during January–February 1979. *Mon. Wea. Rev.,* **113,** 1663–1680.

Bony, S., K.-M. Lau, and Y. C. Sud, 1997: Sea surface temperature and large-scale circulation influences on tropical greenhouse effect and cloud radiative forcing. *J. Climate,* **10,** 2055–2077.

Cess, R. D., and Coauthors, 1996: Cloud feedback in atmospheric general circulation models: An update. *J. Geophys. Res.,* **101,** 12 791–12 794.

Charlock, T. P., and V. Ramanathan, 1985: The albedo field and cloud radiative forcing produced by a general circulation model with internally generated cloud optics. *J. Atmos. Sci.,* **42,** 1408–1429.

Chen, S. S., and R. A. Houze Jr., 1997: Diurnal variation and lifecycle of deep convective systems over the tropical Pacific warm pool. *Quart. J. Roy. Meteor. Soc.,* **123,** 357–388.

Dudhia, J., 1993: A nonhydrostatic version of the Penn State–NCAR mesoscale model: Validation tests and simulations of an Atlantic cyclone and cold front. *Mon. Wea. Rev.,* **121,** 1493–1513.

Duvel, J. P., and F. M. Bréon, 1991: The clear-sky greenhouse effect sensitivity to a sea surface temperature change. *J. Climate,* **4,** 1162–1169.

Ebert, E. E., and J. A. Curry, 1992: A parameterization of ice cloud optical properties for climate models. *J. Geophys. Res.,* **97,** 3831–3836.

Fairall, C. W., E. F. Bradley, D. P. Rogers, J. B. Edson, and G. S. Young, 1996: Bulk parameterization of air–sea fluxes for Tropical Ocean Global Atmosphere Coupled–Ocean Atmosphere Response Experiment. *J. Geophys. Res.,* **101,** 3747–3764.

Fu, Q., S. K. Krueger, and K. N. Liou, 1995: Interactions of radiation and convection in simulated tropical cloud clusters. *J. Atmos. Sci.,* **52,** 1310–1328.

Grabowski, W. W., M. W. Moncrieff, and J. T. Kiehl, 1996: Long-term behaviour of precipitating tropical cloud systems: A numerical study. *Quart. J. Roy. Meteor. Soc.,* **122,** 1019–1042.

Grell, G. A., J. Dudhia, and D. R. Stauffer, 1994: A description of the fifth-generation Penn State/NCAR Mesoscale Model (MM5). NCAR Tech. Note NCAR/TN-398 + STR, 138 pp.

Grenier, H., and C. S. Bretherton, 2001: A moist PBL parameterization for large-scale models and its application to subtropical cloud-topped marine boundary layers. *Mon. Wea. Rev.,* **129,** 357–377.

Hansen, J., G. Russell, A. Lacis, I. Fung, D. Rind, and P. Stone, 1985: Climate response times: Dependence on climate sensitivity and ocean mixing. *Science,* **229,** 857–859.

Harrison, E. F., P. Minnis, B. R. Barkstrom, V. Ramanthan, R. D. Cess, and G. G. Gibson, 1990: Seasonal variation of cloud radiative forcing derived from the Earth Radiation Budget Experiment. *J. Geophys. Res.,* **95,** 18 687–18 703.

Hartmann, D. L., 1994: *Global Physical Climatology.* Academic Press, 411 pp.

——, and E. Recker, 1986: On the diurnal variation of outgoing longwave radiation in the tropics. *J. Climate Appl. Meteor.,* **25,** 800–812.

——, and M. L. Michelsen, 1993: Large-scale effects on the regulation of tropical sea surface temperatures. *J. Climate,* **6,** 2049–2062.

——, and K. Larson, 2002: An important constraint on tropical cloud–climate feedback. *Geophys. Res. Lett.,* **29,** 1951, doi:10.1029/2002GL015835.

——, J. R. Holton, and Q. Fu, 2001a: The heat balance of the tropical tropopause, cirrus and stratospheric dehydration. *Geophys. Res. Lett.,* **28,** 1969–1972.

——, L. A. Moy, and Q. Fu, 2001b: Tropical convective clouds and the radiation balance at the top of the atmosphere. *J. Climate,* **14,** 4495–4511.

Held, I. M., R. S. Hemler, and V. Ramaswamy, 1993: Radiative–convective equilibrium with explicit two-dimensional moist convection. *J. Atmos. Sci.,* **50,** 3909–3927.

Ikawa, M., and K. Saito, 1991: Description of a nonhydrostatic model developed at the forecast research department of the MRI. Tech. Rep. 28.

Janowiak, J. E., P. A. Arkin, and M. Morrissey, 1994: An examination of the diurnal cycle in oceanic tropical rainfall using satellite and in situ data. *Mon. Wea. Rev.,* **122,** 2296–2311.

Kain, J. S., and J. M. Fritsch, 1990: A one-dimensional entraining/detraining plume model and its application in convective parameterization. *J. Atmos. Sci.,* **47,** 2784–2802.

Kiehl, J. T., J. J. Hack, G. B. Bonan, B. A. Boville, B. P. Briegleb, D. L. Williamson, and P. J. Rasch, 1996: Description of the NCAR Community Climate Model (CCM3). NCAR Tech. Note NCAR/TN-420 + STR, 152 pp.

Klemp, J. B., and D. R. Durran, 1983: An upper boundary condition permitting internal gravity wave radiation in numerical mesoscale models. *Mon. Wea. Rev.,* **111,** 430–444.

Krueger, S. K., and S. M. Lazarus, 1998: Intercomparison of multiday simulations of convection during TOGA COARE with several cloud-resolving and single-column models. *Proc. Eighth Atmospheric Radiation Measurement (ARM) Science Team Meeting,* Tucson, AZ, Dept. of Energy, 391–397.

——, and ——, 1999: Intercomparison of multi-day simulations of convection during TOGA COARE with several cloud-resolving and single-column models. Preprints, *23d Conf. on Hurricanes and Tropical Meteorology*, Dallas, TX, Amer. Meteor. Soc., 643–647.

Larson, K., and D. L. Hartmann, 2003: Interactions among cloud, water vapor, radiation, and large-scale circulation in the tropical climate. Part II: Sensitivity to spatial gradients of sea surface temperature. *J. Climate*, **16,** 1441–1455.

——, ——, aand S. A. Klein, 1999: The role of clouds, water vapor, circulation, and boundary layer structure in the sensitivity of the tropical climate. *J. Climate*, **12,** 2359–2374.

Lau, K.-M., C. H. Sui, M. D. Chou, and W. K. Tao, 1994: An inquiry into the cirrus-cloud thermostat effect for tropical sea surface temperature. *Geophys. Res. Lett.*, **21,** 1157–1160.

——, H.-T. Wu, and S. Bony, 1997: The role of large-scale atmospheric circulation in the relationship between tropical convection and sea surface temperature. *J. Climate*, **10,** 381–392.

Li, X., C.-H. Sui, K.-M. Lau, and M.-D. Chou, 1999: Large-scale forcing and cloud–radiation interaction in the tropical deep convective regime. *J. Atmos. Sci.*, **56,** 3028–3042.

Lin, Y.-L., R. D. Farley, and H. D. Orville, 1983: Bulk parameterization of the snow field in a cloud model. *J. Climate Appl. Meteor.*, **22,** 1065–1092.

Lindzen, R. S., M. D. Chou, and A. Y. Hou, 2001: Does the earth have an adaptive infrared iris? *Bull. Amer. Meteor. Soc.*, **82,** 417–432.

Liu, C., and M. W. Moncrieff, 1998: A numerical study of the diurnal cycle of tropical oceanic convection. *J. Atmos. Sci.*, **55,** 2329–2344.

McCaa, J. R., 2001: A new parameterization of marine stratocumulus and shallow cumulus clouds for climate models. Ph.D. dissertation, University of Washington, 161 pp.

Miller, R. L., 1997: Tropical thermostats and low cloud cover. *J. Climate*, **10,** 409–440.

Pierrehumbert, R. T., 1995: Thermostats, radiator fins, and the local runaway greenhouse. *J. Atmos. Sci.*, **52,** 1784–1806.

Ramanathan, V., and W. Collins, 1991: Thermodynamic regulation of ocean warming by cirrus clouds deduced from the 1987 El Niño. *Nature*, **351,** 27–32.

Raval, A., and V. Ramanathan, 1989: Observational determination of the greenhouse-effect. *Nature*, **342,** 758–761.

Reisner, J., R. M. Rasmussen, and R. T. Bruintjes, 1998: Explicit forecasting of supercooled liquid water in winter storms using the MM5 mesoscale model. *Quart. J. Roy. Meteor. Soc.*, **124B,** 1071–1107.

Robe, F. R., and K. A. Emanuel, 1996: Moist convective scaling: Some inferences from three-dimensional cloud ensemble simulations. *J. Atmos. Sci.*, **53,** 3265–3275.

Rossow, W. B., and R. A. Schiffer, 1999: Advances in understanding clouds from ISCCP. *Bull. Amer. Meteor. Soc.*, **80,** 2261–2287.

Rozendaal, M. A., C. B. Leovy, and S. A. Klein, 1995: An observational study of diurnal variations of marine stratiform cloud. *J. Climate*, **8,** 1795–1809.

Rutledge, S. A., and P. V. Hobbs, 1984: The mesoscale and microscale structure and organization of clouds and precipitation in midlatitude cyclones. Part XII: A diagnostic modeling study of precipitation development in narrow cold-frontal rain bands. *J. Atmos. Sci.*, **41,** 2949–2972.

Salathe, E., and D. L. Hartmann, 1997: A trajectory analysis of tropical upper-tropospheric moisture and convection. *J. Climate*, **10,** 2533–2547.

Schiffer, R. A., and W. B. Rossow, 1985: ISCCP global radiance data set: A new resource for climate research. *Bull. Amer. Meteor. Soc.*, **66,** 1498–1505.

Stephens, G. L., 1990: On the relationship between water vapor over the oceans and sea surface temperature. *J. Climate*, **3,** 634–645.

Stocker, T. F., and Coauthors, 2001: Climate processes. *Climate Change 2001: The Scientific Basis*, J. T. Houghton et al., Eds., Cambridge University Press.

Su, H., S. S. Chen, and C. S. Bretherton, 1999: Three-dimensional week-long simulations of TOGA-COARE convective systems using the MM5 mesoscale model. *J. Atmos. Sci.*, **56,** 2326–2344.

Sui, C. H., K. M. Lau, W. K. Tao, M. D. Chou, and J. Simpson, 1993: Simulated water and radiation budgets in the Tropics. Preprints, *20th Conf. on Hurricanes and Tropical Meteorology*, San Antonio, TX, Amer. Meteor. Soc., 431–434.

——, ——, ——, and J. Simpson, 1994: The tropical water and energy cycles in a cumulus ensemble model. Part I: Equilibrium climate. *J. Atmos. Sci.*, **51,** 711–728.

Tompkins, A. M., and G. C. Craig, 1999: Sensitivity of tropical convection to sea surface temperature in the absence of large-scale flow. *J. Climate*, **12,** 462–476.

Udelhofen, P., and D. L. Hartmann, 1995: Influence of tropical convective cloud systems on the relative humidity in the upper troposphere. *J. Geophys. Res.*, **100,** 7423–7440.

Wallace, J. M., 1992: Effect of deep convection on the regulation of tropical sea surface temperature. *Nature*, **357,** 230–231.

Weaver, C. P., W. D. Collins, and H. Grassel, 1994: Relationship between clear-sky atmospheric greenhouse effect and deep convection during the Central Equatorial Pacific Experiment: Model calculations and satellite observations. *J. Geophys. Res.*, **99,** 25 891–25 901.

Wu, X., W. W. Grabowski, and M. W. Moncrieff, 1998: Long-term behavior of cloud systems in TOGA COARE and their interactions with radiative and surface processes. Part I: Two-dimensional modeling study. *J. Atmos. Sci.*, **55,** 2693–2714.

Xu, K.-M., and D. Randall, 1999: A sensitivity study of radiative–convective equilibrium in the Tropics with a convection-resolving model. *J. Atmos. Sci.*, **56,** 3385–3399.

——, A. Arakawa, and S. K. Krueger, 1992: The macroscopic behavior of cumulus ensembles simulated by a cumulus ensemble model. *J. Atmos. Sci.*, **49,** 2402–2420.

Zhang, M. H., J. J. Hack, J. T. Kiehl, and R. D. Cess, 1994: Diagnostic study of climate feedback processes in atmospheric general circulation models. *J. Geophys. Res.*, **99,** 5525–5537.